

# Retinotopic mapping of lateral geniculate nucleus in humans using functional magnetic resonance imaging

WEI CHEN<sup>\*†</sup>, XIAO-HONG ZHU<sup>\*</sup>, KEITH R. THULBORN<sup>‡</sup>, AND KAMIL UGURBIL<sup>\*</sup>

<sup>\*</sup>Center for Magnetic Resonance Research, Radiology Department, University of Minnesota School of Medicine, 2021 Sixth Street SE, Minneapolis, MN 55455; and <sup>‡</sup>MR Research Center, Department of Radiology, University of Pittsburgh Medical Center, B822.1, Presbyterian University Hospital, 200 Lothrop Street, Pittsburgh, PA 15213

Edited by Robert G. Shulman, Yale University, New Haven, CT, and approved January 4, 1999 (received for review November 10, 1998)

**ABSTRACT** Subcortical nuclei in the thalamus, which play an important role in many functions of the human brain, provide challenging targets for functional mapping with neuroimaging techniques because of their small sizes and deep locations. In this study, we explore the capability of high-resolution functional magnetic resonance imaging at 4 Tesla for mapping the retinotopic organization in the lateral geniculate nucleus (LGN). Our results show that the hemifield visual stimulation only activates LGN in the contralateral hemisphere, and the lower-field and upper-field visual stimulations activate the superior and inferior portion of LGN, respectively. These results reveal a similar retinotopic organization between the human and nonhuman primate LGN and between LGN and the primary visual cortex. We conclude that high-resolution functional magnetic resonance imaging is capable of functional mapping of suborganizations in small nuclei together with cortical activation. This will have an impact for studying the thalamocortical networks in the human brain.

Neuronal activity can elevate electromagnetic signal changes along with hemodynamic and metabolic changes (the secondary effects). These changes provide basic detection sources for all modern neuroimaging techniques. Generally, there are two categories of neuroimaging techniques. The first category is based on the detection of electromagnetic signal changes elevated by neuronal activity using single or multiple detection senses surrounding the human head. The representative techniques are: (i) electroencephalography; (ii) event-related potentials, which are based on the electroencephalography measurements synchronized with task executions; and (iii) magnetoencephalography. The second category is based on (i) the detection of hemodynamic changes (cerebral blood flow, cerebral blood volume, and oxygenation) and/or metabolic changes (glucose utilization and oxygen utilization) induced by neuronal activity and (ii) the well-established phenomenon of functional coupling between neuronal activity and these changes (1, 2). The most common techniques in this category are positron emission tomography, single photon emission computed tomography, optical imaging, near infrared spectroscopy, and newly developed functional magnetic resonance imaging (fMRI) (3–5). Although all of these techniques have been used successfully to map functional activation in cortical areas, most are not suitable for detecting and distinguishing activation in numerous nuclei located in the thalamus. As such, subcortical nuclei are integral parts of the human neural networks and play an important role in many brain functions; they provide challenging targets for functional mapping with neuroimaging techniques. The main obstacles are the small nucleus sizes and their deep locations in the thalamus and

limited spatial resolution, detection sensitivity, and penetration depth of neuroimaging techniques. It would be important to explore a unique imaging technique that allows functional mapping of both cortical and subcortical activation in the human brain.

The principle of the fMRI technique is based on blood oxygenation level dependent (BOLD) contrast (6). The magnitude of BOLD change depends on alterations in tissue deoxyhemoglobin content, which is sensitive to changes on the cerebral metabolic rate of oxygen ( $CMR_{O_2}$ ), cerebral blood flow, as well as cerebral blood volume (7, 8). “Uncoupled” alterations in  $CMR_{O_2}$  and cerebral blood flow during functional activation (9–11) would lead to a decrease in regional deoxyhemoglobin content and, ultimately, in magnetic susceptibility gradients across and near the luminal boundaries of blood vessels. This will cause a signal increase in  $T_2^*$  and/or  $T_2$  weighted magnetic resonance (MR) images, which reflects a positive BOLD response. Generally, the magnitude of BOLD change during physiological activation is small (on the order of several percent). However, the origin of the BOLD signal is intravascular and extravascular water, which has an extremely high concentration in the brain. This significantly compensates the small BOLD change and provides high detection sensitivity, which can be enhanced further at high magnetic fields (12–15). This superior detection sensitivity combined with fast MRI techniques provides a capability for functional mapping of the entire human brain with high spatial resolution. In addition, anatomical images with high spatial resolution and superior imaging contrast can be routinely obtained during the same fMRI study and they are important for anatomical assignments of nucleus structures. These advantages make fMRI a possible candidate for detecting small nucleus activation in the thalamus.

The relay function of the lateral geniculate nucleus (LGN) during visual perception processing has been studied extensively (16–20). In addition to the cortical regions involving the occipito-temporo-parietal pathways, visual perception must engage the LGN in the thalamus, as well as areas in the primary visual cortex (V1). Therefore, the LGN provides a suitable target to examine the feasibility of fMRI for detecting the nucleus activation in the thalamus. Recently, it was demonstrated that the fMRI technique could be used to detect the bilateral activation in the human LGN during a full-field visual stimulation (21, 22) and it is capable of detecting the LGN activation reliably in single subjects at 4 tesla (21). Similar to the cortex, the LGN is functionally and spatially segregated and compartmentalized. It is well known that the LGN consists of four parvocellular layers and two magnocellular layers (20). Each layer receives inputs from specific visual fields via retina

This paper was submitted directly (Track II) to the *Proceedings* office. Abbreviations: LGN, lateral geniculate nucleus; V1, primary visual cortex; MRI, magnetic resonance imaging; fMRI, functional MRI; BOLD, blood oxygenation level dependent.

<sup>†</sup>To whom correspondence should be addressed: e-mail: wei@cmrr.umn.edu.

The publication costs of this article were defrayed in part by page charge payment. This article must therefore be hereby marked “advertisement” in accordance with 18 U.S.C. §1734 solely to indicate this fact.

PNAS is available online at [www.pnas.org](http://www.pnas.org).

and then retinotopically projects to V1. The retinotopic organizations in V1 and other associated visual cortical areas have been mapped by using fMRI (23–25). In this study we explore the capability of high-resolution fMRI at a high magnetic field (4 tesla) for mapping the retinotopic organization in the small LGN [ $\approx 5 \times 6 \text{ mm}^2$  cross-section size in the coronal orientation in the human brain (26)]. This goal is achieved by testing whether the fMRI technique can (i) detect the contralateral hemisphere LGN activation during hemifield visual stimulations and (ii) spatially differentiate the functional activation within a single LGN between the upper-field and lower-field visual stimulations.

## MATERIALS AND METHODS

**Visual Stimuli.** The hemifield visual stimulus was made by two checkerboards (model S10VSMA, Grass Instruments, Quincy, MA). For the left–right hemifield visual stimulus, the two checkerboards were horizontally arranged side by side and placed 24 cm from the subject's eyes with  $21.6^\circ$  (width)  $\times 10^\circ$  (height) visual field. There was a narrow dark gap ( $1.6^\circ$ ) between the two checkerboards and a small white circle marker was located at the center of the dark gap as a central fixation point. The checkerboards were reversed at 16 Hz frequency between the red and black colors and could be turned on (or off) simultaneously or independently. For the upper-field and lower-field visual stimuli, the same stimulus for the left–right hemifield visual stimulations was used except for with a  $90^\circ$  rotation; in this case, the visual field was restricted to  $10^\circ$  (width)  $\times 14.2^\circ$  (height) because of the narrow space inside the MRI scanner.

**fMRI Acquisition.** The fMRI studies were performed on a Varian console interfaced to a Siemens (Erlangen, Germany) 4 Tesla whole-body system equipped with a head gradient coil insert. A quadrature head birdcage probe was used for excitation of water resonance and reception of MRI signals. A modified gradient echo-planar imaging sequence with four segments, variable flip angles, center-out k-space sampling, and navigator echo correction (27, 28) was used to acquire high-resolution  $T_2^*$ -weighted fMRI images ( $128 \times 128$  image matrix size,  $20 \times 20 \text{ cm}^2$  field of view, nominal resolution  $1.56 \times 1.56 \text{ mm}^2$ , and 3 mm slice thickness). Five to seven contiguous coronal slices covering LGN were collected, except for one subject who performed the study a second time by using the axial image orientation. Two additional coronal slices covering the calcarine fissure in V1 were also acquired in some subjects for examining the functional relationship between V1 and LGN. The imaging acquisition parameters were 25 msec echo time and 2 sec per multislice image set. Four control periods and four task periods were designed in an interleaved way (4 cycles); 20 image sets were acquired in each of the 8 consecutive periods resulting in a total of 160 multislice image sets for the entire visual stimulation paradigm (5.3 min). Additionally, multislice ( $128 \times 128$  matrix size)  $T_1$ -weighted TurboFLASH images and a three-dimensional MDEFT image data set (29) were acquired for anatomical information. A head motion detector was used to provide an on-line monitor to ensure no head movements during functional studies.

**fMRI Data Analysis.** The acquired fMRI raw data were Gaussian filtered in the k-space for the signal-to-noise ratio enhancement. The Gaussian filter increased pixel sizes at full-width-at-half-maximum by  $\approx 0.3$  pixel in comparison with the full-width-at-half-maximum without the Gaussian filtering inherent in discrete data because of the effect of pixelation (30). The filtered data were Fourier transformed and analyzed by using functional imaging software (STIMULATE) developed in our laboratory. The fMRI maps were generated by comparing the  $T_2^*$ -weighted echo-planar images acquired between task and control periods using the period cross-correlation statistical methods (31). Activation pixels were determined by

the following three criteria. (i) To eliminate false activation pixels in areas of high signal fluctuation, pixels where the standard deviation of image-to-image MR signal fluctuation was  $>3.0$ – $5.0\%$  relative to the mean MR signal during all control periods were excluded from the cross-correlation analysis. This primarily suppressed the pixels at large vessels, cerebrospinal fluid space, and in regions of poor signal-to-noise ratio in echo-planar images (21, 32). (ii) Only pixels with a cross-correlation coefficient above a threshold were included in the functional maps; slightly different cross-correlation coefficient values were used for processing different fMRI data sets that depend on the image quality and the BOLD response and the averaged cross-correlation coefficient value was  $0.29 \pm 0.05$  (SD). (iii) Pixels with less than two contiguous activated pixels were excluded from the functional maps. This threshold of two-pixel cluster size improves the effective statistical significance of the detected “activation” (33). The method described by Xiong *et al.* was used to calculate the effective probability value  $P$  for false positives showing activated pixels (21, 30). This method accounts for (i) the cluster size threshold ( $=2$ ); (ii) the intensity threshold of statistical significance (the  $t$  or  $z$  values) for creating the activated pixels ( $=3.74$ ); (iii) the smoothness due to the Gaussian filtering; and (iv) the total number of pixels in the searched brain area used in the statistical analysis ( $\approx 4,000$  for a single slice). Considering this method (21, 30), the calculated effective  $P$  value was 0.02 compared with the  $P$  value of 0.0002 from the calculation based on the cross-correlation coefficient alone (31).

**Human Experiments.** Two groups of healthy right-handed subjects (assessed by means of the Edinburgh handedness inventory) without history of neurological disorders participated in this study, which was approved by the institutional review board of the University of Minnesota Medical School. The subjects were recruited from the academic university environment.

## RESULTS AND DISCUSSION

**fMRI Mapping of Retinotopic Relationship in LGN Related to Hemifield Visual Stimulations.** The subjects of the first group ( $n = 3$ ; one female and two males, age range 19–29 years) performed a set of visual tasks by using the left–right hemifield stimuli during high-resolution fMRI studies (see *Materials and Methods*). There were four different visual task designs: (i) dark screen vs. full-field visual stimulation, (ii) dark screen vs. left-field visual stimulation, (iii) dark screen vs. right-field visual stimulation, and (iv) left-field vs. right-field visual stimulation. Fig. 1 shows the LGN activation maps superimposed over  $T_1$ -weighted anatomical images for these four visual stimulation tasks performed in the same experimental session from two representative subjects (subjects 1 and 2; the same results were observed in subject 3, who only performed three visual stimulation tasks). The full-field visual stimulation activated LGN bilaterally (Fig. 1*a*); the sizes of the LGN activation varied significantly between the left and right LGN within the same subject and between subjects.

The hemifield retinotopic relationship in the human brain is demonstrated in the LGN activation maps by the other three tasks. The left-field and right-field visual stimulations relative to a dark screen only activated the corresponding contralateral LGN (Fig. 1*b* and *c*). This was further confirmed by the LGN activation maps derived from the alternating left and right hemifield visual stimulation (Fig. 1*d*). In this paradigm, BOLD signal intensity changes associated with “activation” occur out of phase in time for the left and right hemisphere LGN; these two different patterns of activation are represented with two different colors (red vs. purple) in Fig. 1*d*. These results clearly demonstrate that the activation detected at the anatomic location of LGN (21) was responsive only to the contralateral visual field stimulations.

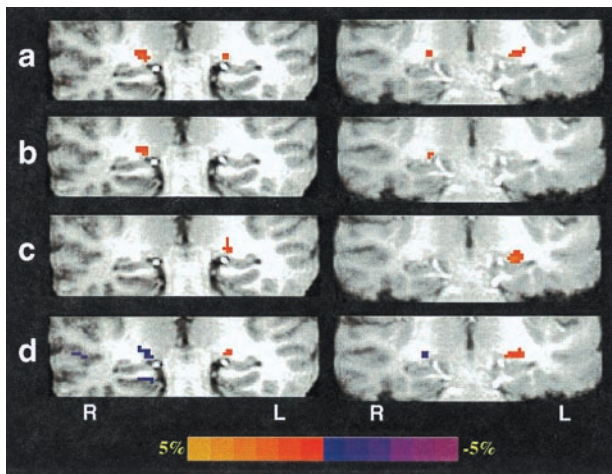


FIG. 1. fMRI mapping of the LGN activation from subject 1 (left column) and subject 2 (right column) during the left-right hemifield visual stimulations. LGN activation maps (coronal image orientation) were generated from: (a) full-field visual stimulation; (b) left-field visual stimulation; (c) right-field visual stimulation; and (d) alternating left-field and right-field visual stimulation, where the colors red and purple identify the LGN activation pixels that responded to the right-field and left-field visual stimulation, respectively. LGN activation appears superior to the hippocampal formation. L and R represent the left and right hemispheres, respectively.

The comparisons of the LGN activation in Fig. 1 illustrate excellent reproducibility of activation locations and sizes (accounting for the activation pixel number) among the four different visual stimulation tasks within the same subjects. This indicates that the fMRI technique at this magnetic field strength provides a reliable and sensitive tool for detecting activation in small subcortical nuclei, in this particular case, within the human thalamus. High magnetic fields are expected to provide advantages of higher BOLD sensitivity to microvasculature, which translates into enhanced spatial specificity in functional brain maps (21, 34, 35). This is supported further by the results presented in Fig. 2, showing activation maps from a different experimental session and imaging orientation for

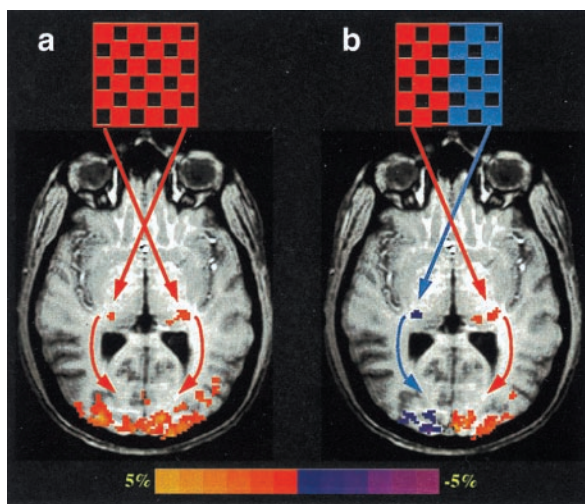


FIG. 2. fMRI mapping of the LGN and V1 activation from subject 2 during the left-right hemifield visual stimulations from a different experimental session and the axial image orientation. (a) LGN activation maps generated from the full-field visual stimulation. (b) LGN activation maps generated from the alternating left and right hemifield visual stimulation. The colors red and purple in *b* indicate the LGN activation pixels that responded to the right and left visual hemifield stimulation, respectively. Arrows show the visual pathway from retinas to LGN and from LGN to V1 in the human brain.

one of the two subjects whose images are shown in Fig. 1 (Right). In this study, the fMRI data were acquired in the axial orientation covering both LGN and V1, whereas the subject experienced either the full-field visual stimulation (Fig. 2a) or the alternating left and right hemifield visual stimulation (Fig. 2b). The activation maps not only demonstrate the same retinotopic relationship as in the first experiment shown in Fig. 1, but also indicate that the sizes of the LGN activation in the different hemispheres are almost identical between the two experiments for the same subject.

The average BOLD signal intensity change calculated from the LGN activation pixels of the coronal fMRI maps was  $2.2 \pm 0.5\%$  (number of experiments;  $n = 14$ ). This is significantly higher than the 1.1% observed from our previous study with lower resolution fMRI (21). This result is expected from partial volume effects when true activation volumes are smaller than imaging volume elements (35). An approximately 7-fold decrease of voxel size in this high-resolution fMRI study relative to our earlier work (21) significantly reduces the partial volume effect and leads to an increase of BOLD signal. The average number of the LGN activation pixels in the coronal orientation was  $8.6 \pm 4.5$ . This gives, approximately, the two-dimensional LGN activation sizes of  $4.6 \times 4.6 \text{ mm}^2$  (ignoring Gaussian filter broadening) and  $5.1 \times 5.1 \text{ mm}^2$  (including Gaussian filter broadening), respectively. This result is consistent with the anatomical study showing approximately  $5 \times 6 \text{ mm}^2$  sizes of LGN in the coronal orientation in the human brain (26).

**fMRI Mapping of Retinotopic Relationship in LGN Related to Upper-Field and Lower-Field Visual Stimulations.** The subjects of the second group ( $n = 5$ ; two males and three females, average age  $27 \pm 8$  years) performed another set of visual tasks using the upper-field and lower-field visual stimuli. Two visual tasks were designed: (i) dark screen vs. the upper-field visual stimulation and (ii) dark screen vs. the lower-field visual stimulation. These tasks are expected to activate LGN bilaterally. However, the most striking question is whether the retinotopic relationship reflecting the upper vs. lower visual field can be detected and distinguished within a single small LGN by using high-resolution fMRI at high magnetic fields.

Fig. 3a contains the fMRI maps showing the LGN activation during the upper-field and lower-field visual stimulation (relative to a dark control state), respectively, from a representative subject (subject 4). LGN was activated bilaterally in both cases; however, the central positions of the LGN activation were significantly shifted, predominantly in the superior direction. The LGN activation induced by the upper-field visual stimulation was more inferior in location (closer to the hippocampal formation), as shown in Fig. 3a (Left Inset) compared with the LGN activation induced by the lower-field visual stimulation (Fig. 3a Right Inset). There was partial overlap of the LGN activation between the upper-field and lower-field visual tasks.

Spatial differentiation of activation within LGN between the two tasks is better visualized by using fMRI maps that are composites of the two activation maps generated with the upper-field and lower-field visual stimulations relative to a dark control state. Such maps are shown for four different subjects in Fig. 3b. In this figure, the colors yellow and green represent the LGN activation corresponding to stimulation in the lower and upper visual fields, respectively, relative to a dark control state; the color red represents the overlap, i.e., pixels activated by both tasks. One of the five subjects examined did not show significant activation in the right hemisphere LGN during one task; consequently, composite fMRI maps from only four subjects are presented (Fig. 3b). One of the four subjects whose images are presented in Fig. 3b performed these tasks two times at different experimental sessions; the results were similar for the two sessions. Generally, the spatial locations of activation in the LGN region induced by the

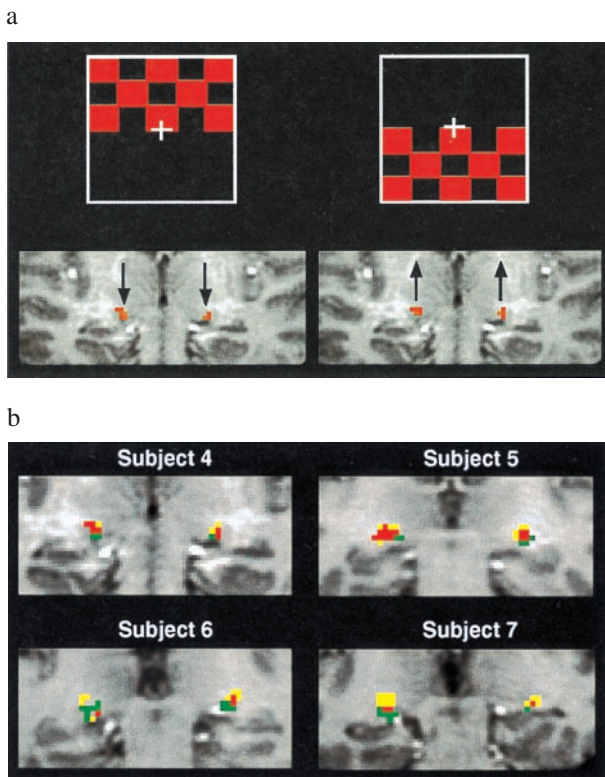


**FIG. 3.** fMRI mapping of the LGN activation during the upper-field and lower-field visual stimulations (coronal image orientation). (a) fMRI maps generated from the upper-field visual stimulation (the left fMRI map and the upper red checkerboard inset) and from the lower-field visual stimulation (the right fMRI map and the lower red checkerboard inset) of a representative subject (subject 4). Arrows show the vertical direction of spatial shifting of the LGN activation during the upper-field and lower-field visual stimulation, respectively. (b) Composite fMRI maps of the LGN activation from four subjects obtained by combining the two activation maps generated from the upper-field and lower-field visual stimulations relative to a dark control state. Green and yellow pixels represent the LGN activation pixels induced by the upper-field and lower-field visual stimulation, respectively. Red pixels represent the overlap LGN activation pixels between the upper-field and lower-field visual stimulations.

upper-field and lower-field visual stimulations were consistent for intrasubject comparisons between the left and right hemisphere LGN. There was, however, some variation in the LGN activation size and shape among the different subjects. These results are consistent with earlier observations of large anatomical variability in the human LGN size (36, 37).

The LGN activation maps in Fig. 3*b* illustrate that the upper visual field projects to the inferior portion of LGN and the lower visual field projects to the superior portion of LGN. To the best of our knowledge, this is the first demonstration of a retinotopic relationship within the LGN in the human brain. Our results from the retinotopic mapping in the human LGN are consistent with the retinotopic organization reported for a nonhuman primate visual system that has been studied extensively by using microelectrode recording (38) and selective lesions (39, 40). These nonhuman primate studies have shown that the superior and inferior portions of LGN represent the lower and the upper visual fields, respectively, in the contralateral hemifield. Our results also illustrate that the LGN retinotopic organization behaves similarly to V1 (24) with respect to upper and lower visual fields in humans. The upper and lower visual field representations in V1 are anatomically separated by the calcarine fissure and as such are spatially distinguishable without overlap. In contrast, they are continuous in each of the LGN layers. This makes it difficult to

completely separate the spatial locations of the LGN activation between the upper-field and lower-field visual stimulations using current spatial resolution of fMRI. This partially contributes to the overlap of the LGN activation between the upper and lower visual fields. It may be possible to reduce further this overlap using higher resolution fMRI. The image signal loss caused by the decrease of image pixel volume in higher resolution fMRI can be compensated by the BOLD signal increase due to less partial volume effects as shown here and in ref. 35.

**General Discussion.** At high magnetic fields, the spatial resolution and specificity of the fMRI technique have been shown to exist at the ocular dominance column level (41). However, the visual cortex represents a favorable target in fMRI studies because it can be studied with surface coils, which provide much improved signal-to-noise ratio compared with coils that must circumscribe the head for entire brain studies or for detecting subcortical regions. Surface coil detection was indispensable for the ocular dominance column studies (41) and was also employed in retinotopic mapping of V1 (24). In this paper, we have demonstrated that high-resolution functional imaging by fMRI extends to mapping suborganizations within small subcortical nuclei in the thalamus. This in turn indicates that it will be possible to study large-scale neural networks (42) encompassing both cortical and subcortical gray matter in single human subjects at a relatively high resolution. Fig. 2 provides a demonstration showing a simple thalamocortical network of the lower-order visual system (LGN and V1) related to retinotopic relationships during visual stimulations.

The connection between fMRI and neuronal activity is due to a tightly functional coupling between neuronal activity and hemodynamic or metabolic response (1, 43, 44). One interesting issue is the spatial correlation between the activation locations detected by fMRI and sites of neuronal activity. Recently, it has been shown that the spatial distribution of the BOLD signal induced by whisker stimulation in the rat brain has the same spatial pattern and dimension as that of neuronal electrical activity in a single whisker barrel (45). This is supported by our human brain study showing excellent consistencies of the LGN locations and sizes between anatomical image and fMRI maps. It indicates that the spatial specificity of fMRI is capable of mapping small nuclei in the millimeter domain.

## CONCLUSIONS

We have demonstrated the feasibility of high-resolution fMRI at 4 Tesla for mapping the retinotopic organization in the small LGN in the human thalamus. The results reveal a similar retinotopic relationship between the human and nonhuman primate LGN and between LGN and V1. The high-resolution fMRI technique is capable of functional mapping of suborganizations in small nuclei and it provides a unique and reliable method for detecting functional activation covering both cortical areas and subcortical nuclei of the entire human brain without multiple subject averaging. Such fMRI capability will be vital to understanding the human brain functions related to sensory perception and higher cognitive processing (46) at both physiological and pathological conditions.

We thank J. T. Voyvodic, C. Martin, and D. Davis for their interest and initial support for starting this project; P. Andersen, S.-G. Kim, J. Strupp, and G. Adriany for technical assistance and discussion; and J. C. Horton for the communication about the LGN anatomy (W.C.). This research was supported by National Research Resource (National Institutes of Health) Grant P41 RR08079 and National Institutes of Health Grant NS 38070 (W.C.).

1. Raichle, M. E. (1987) in *Handbook of Physiology: The Nervous System*, eds Mountcastle, V. B., Plum, F. & Geiger, S. R. (Am. Physiol. Soc., Bethesda, MD), pp. 643–674.
2. Sokoloff, L. (1981) *J. Cereb. Blood Flow Metab.* **1**, 7–36.
3. Ogawa, S., Tank, D. W., Menon, R., Ellermann, J. M., Kim, S.-G., Merkle, H. & Ugurbil, K. (1992) *Proc. Natl. Acad. Sci. USA* **89**, 5951–5955.
4. Kwong, K. K., Belliveau, J. W., Chesler, D. A., Goldberg, I. E., Weisskoff, R. M., Poncelet, B. P., Kennedy, D. N., Hoppel, B. E., Cohen, M. S., Turner, R., *et al.* (1992) *Proc. Natl. Acad. Sci. USA* **89**, 5675–5679.
5. Bandettini, P. A., Wong, E. C., Hinks, R. S., Tikofsky, R. S. & Hyde, J. S. (1992) *Magn. Reson. Med.* **25**, 390–397.
6. Ogawa, S., Lee, T.-M., Nayak, A. S. & Glynn, P. (1990) *Magn. Reson. Med.* **14**, 68–78.
7. Ogawa, S., Menon, R. S., Tank, D. W., Kim, S.-G., Merkle, H., Ellermann, J. M. & Ugurbil, K. (1993) *Biophys. J.* **64**, 800–812.
8. Thulborn, K. R., Waterton, J. C., Matthews, P. M. & Radda, G. K. (1982) *Biochim. Biophys. Acta* **714**, 265–270.
9. Fox, P. T. & Raichle, M. E. (1986) *Proc. Natl. Acad. Sci. USA* **83**, 1140–1144.
10. Fox, P. T., Raichle, M. E., Mintun, M. A. & Dence, C. (1988) *Science* **241**, 462–464.
11. Ribeiro, L., Kuwabara, H., Meyer, E., Fujita, H., Marrett, S., Evans, A. & Gjedde, A. (1993) in *Quantification of Brain Function in Tracer Kinetics and Image Analysis in Brain PET*, ed. Uemura, K. (Elsevier Science, New York), pp. 229–236.
12. Ellermann, J., Garwood, M., Hendrich, K., Hinke, R., Hu, X., Kim, S.-G., Menon, R., Merkle, H., Ogawa, S. & Ugurbil, K. (1994) in *NMR in Physiology and Medicine*, ed. Gillies, R. (Academic, San Diego), pp. 137–150.
13. Ugurbil, K., Ogawa, S., Menon, R., Kim, S.-G., Hu, X., Hinke, R., Ellermann, J., Hendrich, K., Merkle, H., Andersen, P., *et al.* (1994) in *New Horizons in Neuropsychology*, ed. Sugushita, M. (Elsevier Science, Amsterdam), pp. 3–22.
14. Gati, J. S., Menon, R. S., Ugurbil, K. & Rutt, B. K. (1997) *Magn. Reson. Med.* **38**, 296–302.
15. Turner, R., Jezzard, P., Wen, H., Kwong, K. K., Le Bihan, D., Zeffiro, T. & Balaban, R. S. (1993) *Magn. Reson. Med.* **29**, 277–279.
16. Wiesel, T. N. & Hubel, D. H. (1966) *J. Neurophysiol.* **29**, 1115–1156.
17. Hubel, D. H. & Wiesel, T. N. (1966) *Proc. Natl. Acad. Sci. USA* **55**, 1345–1346.
18. Hubel, D. H. & Wiesel, T. N. (1972) *J. Comp. Neurol.* **146**, 421–450.
19. Rakic, P. (1976) *Nature (London)* **261**, 467–471.
20. Zeki, S. (1993) *A Vision of the Brain* (Blackwell Scientific, Oxford).
21. Chen, W., Kato, T., Zhu, X. H., Strupp, J., Ogawa, S. & Ugurbil, K. (1998) *Magn. Reson. Med.* **39**, 89–96.
22. Buchel, C., Turner, R. & Friston, K. (1997) *Magn. Reson. Med.* **38**, 691–694.
23. Engel, S. A., Glover, G. H. & Wandell, B. A. (1997) *Cereb. Cortex* **7**, 181–192.
24. Sereno, M. I., Dale, A. M., Reppas, J. B., Kwong, K. K., Belliveau, J. W., Brady, T. J., Rosen, B. R. & Tootell, R. B. (1995) *Science* **268**, 889–893.
25. DeYoe, E. A., Garman, G. J., Bandettini, P., Glickman, S., Wieser, J., Cox, R., Miller, D. & Neitz, J. (1996) *Proc. Natl. Acad. Sci. USA* **93**, 2382–2386.
26. Horton, J. C., Landau, K., Maeder, P. & Hoyt, W. F. (1990) *Arch. Neurol.* **47**, 1201–1206.
27. Mansfield, P. (1977) *J. Phys. C Solid State Phys.* **10**, L55–L58.
28. Kim, S. G., Hu, X., Adriany, G. & Ugurbil, K. (1996) *Magn. Reson. Med.* **35**, 895–902.
29. Lee, J.-H., Menon, R., Andersen, P., Truwit, C., Garwood, M. & Ugurbil, K. (1995) *Magn. Reson. Med.* **34**, 308–312.
30. Xiong, J., Gao, J. H., Lancaster, J. L. & Fox, P. T. (1995) *Hum. Brain Mapp.* **3**, 287–301.
31. Bandettini, P. A., Jesmanowicz, A., Wong, E. C. & Hyde, J. S. (1993) *Magn. Reson. Med.* **30**, 161–173.
32. Kim, S.-G., Hendrich, K., Hu, X., Merkle, H. & Ugurbil, K. (1994) *NMR Biomed.* **7**, 69–74.
33. Forman, S. D., Cohen, J. D., Fitzgerald, M., Eddy, W. F., Mintun, M. A. & Noll, D. C. (1995) *Magn. Reson. Med.* **33**, 636–647.
34. Menon, R. S., Kim, S. G., Hu, X., Ogawa, S. & Ugurbil, K. (1994) in *Diffusion and Perfusion Magnetic Resonance Imaging*, ed. Le Bihan, D. (Raven, New York), pp. 327–334.
35. Thulborn, K. R., Chang, S. Y., Shen, G. & Voyvodic, J. T. (1997) *NMR Biomed.* **10**, 183–190.
36. Andrews, T. J., Halpern, S. D. & Purves, D. (1997) *J. Neurosci.* **17**, 2859–2868.
37. Hickey, T. L. & Guillery, R. W. (1979) *J. Comp. Neurol.* **183**, 221–246.
38. Malpeli, J. G. & Baker, F. H. (1975) *J. Comp. Neurol.* **161**, 569–594.
39. Schiller, P. H., Logothetis, N. K. & Charles, E. R. (1990) *Visual Neurosci.* **5**, 321–346.
40. Schiller, P. H., Logothetis, N. K. & Charles, E. R. (1990) *Nature (London)* **343**, 68–70.
41. Menon, R. S., Ogawa, S., Strupp, J. P. & Ugurbil, K. (1997) *J. Neurophysiol.* **77**, 2780–2787.
42. Mesulam, M. M. (1998) *Brain* **121**, 1013–1052.
43. Jueptner, M. & Weiller, C. (1995) *Neuroimage* **2**, 148–156.
44. Sokoloff, L. (1981) *Fed. Proc.* **40**, 2311–2316.
45. Yang, X., Hyder, F. & Shulman, R. G. (1997) *Magn. Reson. Med.* **38**, 874–877.
46. Chen, W., Kato, T., Zhu, X. H., Ogawa, S., Tank, D. W. & Ugurbil, K. (1998) *NeuroReport* **9**, 3669–3674.